The mechanism of Mg diffusion in forsterite and the controls on its anisotropy

Joshua M. R. Muir[*1,2], Feiwu Zhang[1] and Andrew M. Walker[2,3]

1) State Key Laboratory of Ore Deposit Geochemistry, Institute of Geochemistry, Chinese Academy of Sciences, Guiyang, 550081, China

2) School of Earth and Environment, University of Leeds, LS2 9JT, United Kingdom

3) Now at: Department of Earth Sciences, University of Oxford, South Parks Road, Oxford OX1 3AN, United Kingdom

*Corresponding author: j.m.r.muir@mail.gyig.ac.cn, andrew.walker@earth.ox.ac.uk, zhangfeiwu@mail.gyig.ac.cn

ORCIDs: Joshua M. R. Muir: 0000-0002-0879-4373, Feiwu Zhang: 0000-0002-4979-0790, Andrew M. Walker : 0000-0003-3121-3255

Abstract

Mg diffusion is important for explaining many properties of forsterite but its mechanism is unknown. This makes it hard to predict how it will behave in different circumstances. In this study we used Density Functional Theory (DFT) and a Kinetic Monte Carlo (KMC) method to calculate the diffusivity of Mg vacancies and interstitials in forsterite and thus the diffusion rate of Mg in forsterite. We predict vacancy diffusion to be highly anisotropic with considerably faster diffusion in the [001] direction while interstitial diffusion is predicted to be more isotropic. Thus we predict that a combination of interstitial and vacancy diffusion is required to reproduce experimentally derived anisotropies. Interstitial diffusion is predicted to be highly pressure dependant such that with increasing pressure the anisotropy of Mg diffusion decreases while temperature has little effect on this anisotropy. Impurities like Fe and water likely cause increases in Mg diffusion rate through the creation of extrinsic Mg vacancies and we predict that without modifications to the inherent mobility of Mg vacancies these cause small increases to diffusional anisotropy at 1300 and 1600 K but very large increases at 1000 K. The activation volume of Mg self diffusion is also predicted to decrease with increasing extrinsic vacancy concentration.

Keywords: Forsterite; Mg Diffusion; DFT

Word Count: 7030

1 Introduction

Diffusion of cations occupying the octahedral metal sites in olivine controls processes that are active in the Earth's crust and upper mantle, and which underpin a range of geophysical and geochemical techniques. In the upper mantle, where olivine with composition close to $(Mg_{0.9},Fe_{0.1})_2SiO_4$ is the dominant phase, the diffusivity of Mg is important in understanding electrical conductivity (Fei et al., 2018, Yoshino et al., 2009, Yoshino et al., 2017, Schock et al., 1989) and could influence deformation even though Mg is a rapidly diffusing species (Jaoul (1990). Anisotropic Mg diffusion could be an important factor in explaining the anisotropic conduction seen in high conductivity layers underneath young oceanic plates (Fei et al., 2018) and, if Mg diffusion is important in forming olivine textures, could also help explain the variety of textures that are formed by olivine under different conditions (Karato et al., 2008). Mg-Fe interdiffusion occurring in zoned phenocrysts from volcanic products is increasingly used as a petrological tool (diffusion chronometry) to understand the timescales of pre-eruptive processes operating in the days and weeks prior to eruption (e.g. Hartley et al. 2016 and Pankhurst et al. 2018). On a longer timescale diffusion-controlled exchange between Mg and Fe in olivine and spinel can be used to infer the post-crystallisation thermal history of ultramafic igneous bodies (Ozawa, 1984). Diffusion can also lead to magnesium and iron isotope fractionation (Teng et al., 2011).

Our understanding and ability to model all of these processes relies upon accurate determination of the Mg self-diffusion and Fe-Mg interdiffusion coefficients in olivine and thus this has been the focus of a range of experimental and computational studies reviewed by Chakraborty (2010). Generally there is a broad agreement as to the Mg self diffusion parameters in forsterite though there is around half an order of magnitude discrepancy between different experimental predictions (Andersson et al., 1989, Chakraborty et al., 1994, Fei et al., 2018, Jollands et al., 2020, Morioka, 1981). Mg self-diffusion is found to be mildly anisotropic with diffusion along [001] found to be up to an order of magnitude

faster than diffusion along [100] and [010] (Andersson et al., 1989, Chakraborty et al., 1994, Jollands et al., 2020). The activation volume for diffusion has been measured as 1-3.5 cm^3/mol (Chakraborty et al., 1994) or 4.0-4.6 cm^3/mol (Fei et al., 2018) which is small in both cases suggesting pressure has little effect on the diffusion rate. So far, however, a mechanistic model of Mg diffusion has not been produced which limits our ability to extend Mg diffusion to novel conditions and to make confident predictions as to its rate in various upper mantle conditions. Details of the diffusion process, such as the origin of diffusional anisotropy and the variation of this anisotropy with pressure, temperature and composition, can also be elucidated with a full mechanism. Thus in this work we studied the atomistic mechanisms of Mg self-diffusion using *ab initio* calculations.

Previously the nature of intrinsic defects (Wright and Catlow, 1994, Braithwaite et al., 2003, Brodholt, 1997) has been studied using interatomic potentials, embedded clusters and Density Functional Theory (DFT) while their mobility (Walker et al., 2009, Bejina et al., 2009, Jaoul et al., 1995) in forsterite have been studied using interatomic potentials. While these two questions are critical for determining cationic mobility in forsterite these studies have neglected important effects. First, interatomic potentials often behave poorly in unusual geometries and these are often formed during diffusion. Second, these studies consider only activation energies and not the time taken for diffusing point defects to overcome these barriers. Third, these studies do not convert their diffusion pathways into a macroscopic diffusion model and thus calculate rates of diffusion. Thus there exists no detailed exploration of Mg diffusion in forsterite using electronic structure methods. In this work we shall examine a possible mechanism for this diffusion. To simplify the discussion we shall consider only the Mg-end member of the olivine solid solution (forsterite) and we shall only explicitly calculate the effect of intrinsic defects without the effect of extrinsic defects arising from impurities.

2 Methods

Diffusion operates on a much longer timescale than is typically accessible by direct atomic simulations. Thus instead of simulating diffusion directly, we instead examine some rare events that are key to

79 diffusion – hops of a point defect between adjacent sites. Repeated occurrences of these hops leads
80 to a random walk of the defect and bulk self-diffusion (Tilley, 1987). Our approach to simulating Mg
81 diffusion in forsterite follows three steps. First, we make use of density functional theory to determine
82 the structure and relative stability of Mg point defects in forsterite. These models represent the
83 ground state end-points of the hops leading to diffusion. Second, we probe the energy landscape that
84 must by traversed by the defect during a hop. This provides us with the energy barrier that must be
85 overcome for the hop to proceed and the structure of the transition state (the configuration with the
86 maximum energy on the minimum energy pathway between the start and the end point). Boltzmann
87 statistics tell us how likely it is for a point defect to have enough energy at a given temperature to
88 overcome the energy barrier while simulation of the lattice vibrations of the ground and transition
89 states allow us to calculate the frequency at which each hop is attempted. Third, we combine
90 information about multiple hops between different ground states using a kinetic Monte Carlo
91 approach to access timescales long enough to observe the random walk and measure Mg diffusion in
92 forsterite.

93 *2.1 Defect calculations using density functional theory and defect concentrations*

94 All input parameters to our models of magnesium diffusion in forsterite are derived from plane wave
95 density functional theory (DFT; Hohenberg and Kohn, 1964; Kohn and Sham, 1965) which allows us to
96 probe the energy periodic boxes of simulated atoms. This was used to evaluate the ground state
97 defect structures and energies, the structures and energies of the transition states, and the way atoms
98 vibrate in these configurations. This approach allows us to calculate the hop activation energies and
99 rates as a function of temperature and pressure. These calculations were undertaken using version
100 16.11 of the CASTEP code (Clark et al., 2005). Full details of the simulation parameters are given in
101 the Supplementary Information but in short we placed Mg, Si and O vacancies in (2x1x2) forsterite
102 super cells and determined their energy as well as the energy of defect-free forsterite. This was done
103 both statically and at temperature, using quasi-harmonic approximation and linear displacement
104 techniques to determine the thermal energies. This was done at 0, 5, 10 and 15 GPa and at static (~0

K), 1000, 1300, 1500, 1600 and 2000 K. Knowing the energy of each defect relative to forsterite we can then calculate the difference in energy between defect-containing and defect-free forsterite for each type of defect and use these to calculate a series of defect producing reactions such as the Mg Frenkel reaction $Mg_{Mg}^{X} \rightarrow V_{Mg}'' + Mg_{I}^{\bullet\bullet}$. We then determine the equilibrium position of these reactions by minimizing the free energy of forsterite (see Supplementary Information) which gives us the equilibrium concentration of defects.

2.2 Defect Hopping

Once ground state structures, energies and concentrations for the defects had been determined, we enumerated the possible hops (where a defect moves from location to location) for V_{Mg}'' and $Mg_{I}^{\bullet\bullet}$ and for each hop we determined its pathway, its transition state structure and its activation energy. We did this by using a constrained optimisation approach. We first determined an approximate path for the hop (for vacancy diffusion this consists of two vacancies with a Mg atom at a point between the vacancies, for interstitial diffusion the interstitial atom is located between stable interstitial sites). For each hop we tried multiple paths, but direct paths proved to have the lowest transition state energy in all cases. A path was defined by at least 10 images (with the Mg atom in different locations between the start and end point) and each image was relaxed with the migrating Mg fixed to the path by preventing its movement in one direction ([100] or [010] or [001]) with the fixed direction being that which has the longest distance along the path. This provides an energy profile along the path and a maximum energy point. We then searched for the transition state by moving along the path from the maximum energy point in 0.1 Å steps in both directions until a maximum was found. This is the candidate transition state. While this method may not definitely find the transition state our frequency calculations (Supplementary Information) typically returned a single imaginary eigenvalue of the dynamical matrix, as expected for a transition state. In the few cases where this was not the case (all for interstitial diffusion) the candidate transition state was found by manual adjustment based on visualising the eigenvectors of the imaginary phonon frequencies until a single imaginary eigenvalue was found. It turned out that this manual adjustment changed the activation energy of

the hop by <0.01 eV suggesting that the constrained optimisation method is highly reliable for finding activation energies even if they are in complex parts of the energy hypersurface.

To determine the rate of hopping we used lattice dynamics (Supplementary Information) to probe the vibration of atoms around the point defects in their ground state and transition state configurations. This allows us to model the effect of temperature on point defect mobility. The rate, *k*, at which a defect hops from one location to another is given by:

$$k = vexp\left(\frac{\Delta S_m}{k_B}\right) exp\left(-\frac{\Delta H_m}{k_B T}\right)$$ Equation 1

where v is the attempt frequency (in Hz) and the two exponential terms are the activation entropy and the activation enthalpy, respectively. The activation enthalpy term was calculated from our constrained optimisation. In order to calculate the attempt frequency and activation entropy we used Vineyard theory (Vineyard, 1957) which is based on absolute rate theory. Both of the temperature-based factors (vibrational entropy and attempt frequency) are combined into a modified attempt frequency (v*) which is found from the ratio of the calculated phonon frequencies:

$$v^* = vexp\left(\frac{\Delta S}{k_B}\right) = \frac{\prod_{j=1}^{N} \nu_j}{\prod_{j=1}^{N-1} \nu_{j'}}$$ Equation 2

where ν_j are the lattice frequencies of a defect in its stable starting position and ν_j' are the real lattice frequencies of the defect at the transition state of its hop. The latter has one imaginary frequency and so one less real frequency. Similar to our treatment of thermal expansion, this theory assumes harmonic small oscillations near the saddle point and thus assumes the system operates as a harmonic oscillator. The rate of each hop is thus determined from its activation energy (determined from the energy of the transition state) and its modified attempt frequency.

2.3 From defects to diffusion

The self-diffusion of Mg by a vacancy mechanism can be represented by:

$$D_{Mg}^{sd-vac} = D_{Mg}^{Vac} N_{Vac}$$ Equation 3

Where D_{Mg}^{Vac} is the diffusion coefficient of Mg vacancies and N_{Vac} is the atomic fraction of Mg vacancies. A similar mechanism applies for diffusion by an interstitial mechanism. As shown below, our atomic scale simulations suggest that diffusion of both interstitials and vacancies can be important for magnesium diffusion in pure forsterite. To account for this possibility, we use the assumption that vacancies and interstitials diffuse independently of each other, which means that the total self-diffusion of Mg in forsterite is given by:

$$D_{Mg}^{sd} = D_{Mg}^{Vac} N_{Vac} + D_{Mg}^{Int} N_{Int}$$ Equation 4.

Other diffusing species not considered in this paper, such as hydrated vacancies, would have their own term if present. The concentration terms in Equation 4 are determined by varying the progress of defect forming reactions – specifically the Mg Frenkel reaction as discussed in the text – until the free energy is minimised (Section 2.1).

Determining the diffusion coefficients for the individual defect species is more complex. For systems with simple geometry, the diffusion coefficients can be found analytically from the attempt frequency, the migration entropy, the activation energy and the crystal structure. For example, for a single hop, the coefficient is given by (Poirier, 1985):

$$D_{Mg}^{Vac} = \frac{\alpha}{q} l^2 v exp\left(\frac{\Delta S_m}{k_B}\right) exp\left(-\frac{\Delta H_m}{k_B T}\right)$$ Equation 5

where α is a geometric prefactor to account for the degeneracy of the hop, *q* is a dimensionality constant (*q* = 2, 4 or 6 for 1, 2 or 3D diffusion), *l* is the length of the hop and the two exponential terms are the activation entropy and the activation enthalpy, respectively. This approach has been used to determine diffusion coefficients in a number of minerals including MgO, bridgmanite and post-perovskite (e.g. Vocaldo et al. 1995; Ammann et al. 2010). However, diffusion in forsterite involves defects moving from one site to an inequivalent site via multiple different hops and so it becomes cumbersome to attempt to develop equations of this type. Instead we seek a numerical estimate of the diffusion coefficients by implementing a kinetic Monte-Carlo (KMC; Bortz et al. (1975)) simulation of the motion of a defect in a forsterite crystal.

First developed to allow the efficient simulation of Ising spin systems, KMC works by simulating the time evolution of a system between a collection of states, with transitions between states governed by a set of rules that includes a probability of that transition occurring in a given amount of time. Transitions between states are selected randomly (preserving the relative probability of each transition) and a clock is advanced by an appropriate amount after the state transition has been determined. This makes it useful for simulating complex transitions with many possible motions as the properties of each transition can be calculated independently and then put collectively into a KMC algorithm. KMC has found a number of applications in extending atomic scale simulations to macroscopic behaviour, including the simulation of dislocation motion (Bulatov and Cai, 2006), chemical vapour deposition (Bagatur'yants et al., 2003) and point defect diffusion (Voter, 2007).

For our simulations, we followed the rejection-free residence time method of Voter (2007). A brief overview of this method is given here, with more detail in the Supplementary Information. For each state in the system (e.g. a vacancy on M1) we enumerate all possible hops from that state and then calculate the rate of each hop (k^i) (section 2.2, equation 1 using equation 2), the sum of the rates of all the hops (k^{tot}) and the probability of each hop occurring $p^i = \frac{k^i}{k^{tot}}$. We then use the weighted probability of each hop to randomly select a hop. We also randomly select a time for that hop to occur (the escape time):

$$t^i = -\left(\frac{1}{k_{tot}}\right) \ln (r^2) \quad \text{Equation 6}$$

Where r^2 is a pseudo-random number drawn from a uniform distribution between 0 (inclusive) and 1 (exclusive) which can be represented as [0,1). At each stage of the calculation the randomly selected hop moves our defect a certain distance in a certain direction and the randomly determined escape time advances the clock. Thus, as this algorithm progresses, we build a list of positions of the defect as a function of time as it undergoes a random walk through the (infinite) crystal structure. We then calculate the mean-squared displacement (MSD) of our defect (using the method of Leetmaa and

Skorodumova (2015) as explained in the supplementary information) as a function of time. This can then be converted to diffusion:

$\langle x^2 \rangle = qDt$ Equation 7

Where q is the dimensionality constant as above.

3 Results

3.1 Crystal structure of olivine

In order to understand and discuss diffusion in forsterite we must first consider its crystal structure. The highly anisotropic crystal structure of forsterite leads to its diffusional anisotropy. Forsterite's distorted hexagonal close packed oxygen sublattice contains two distinct octahedrally co-ordinated M sites: M1, on an inversion centre, and the less symmetric M2, which sits on a mirror plane. M1 sites share edges and form continuous chains along [001] while M2 sites are isolated from each other (sharing an edge with an M1 site and corners with other M1 and M2 sites). This structural anisotropy hits at a possible reason for the directional dependence of Mg diffusion in forsterite: vacancy mobility along chains of M1 sites could be high compared to more tortuous pathways between M1 and M2 sites (Brodholt, 1997, Bejina et al., 2009, Jaoul et al., 1995, Walker et al., 2009). There are also two normally unoccupied octahedral sites in the forsterite structure. Each is located half way between two occupied M sites (and shares faces with them) along [100]. We call the unoccupied octahedral site midway between two M1 sites I1, and the unoccupied octahedral site midway between two M2 sites I2.

3.2 Defect Energies and Concentrations

There are two sites for Mg vacancies in forsterite – the M1 and the M2 sites. We calculate that M1 sites are strongly favoured over M2 sites with pressure increasing the vacancy preference for M1 sites (Table S1). This preference for M1 over M2 vacancies agrees with previous calculations though there

is some difference in the energy of this preference (0.9-1.2 eV in this work, ~1.9 eV with forcefield calculations (Walker et al., 2009) or ~0.8 eV previously using DFT (Brodholt, 1997)).

We have also considered Mg interstitials. As with Walker et al. (2009) we found that the most stable position is a split interstitial at the M1 site with 2 Mg atoms displaced from the centre of this site in opposite [010] directions (shown in Figure S1). This arrangement is very stable with alternative arrangements of the Mg at this site all relaxing into this one. Even placing a Mg atom in an I1 site causes it to relax into this split interstitial arrangement. The other stable configuration is found by placing an additional Mg in the I2 site. The Mg interstitial in the I2 site has an octahedral coordination like the M1 and M2 and is thus geometrically similar to them. At 0 GPa the split M1 interstitial is slightly favoured over the I2 arrangement (~0.2 eV) but with increasing pressure the I2 configuration is favoured (Table S1) as the split M1 arrangement is larger than the I2 arrangement. In QM-MM embedded cluster calculations (Walker et al., 2009) the split M1 geometry was found to be favoured over an I1 interstitial geometry by ~4.4 eV but an I2 geometry was not reported. In our own forcefield calculations we were unable to stabilise an I2 arrangement as I2 arrangements always relaxed into M1 arrangements. Forcefields are thus likely poor at representing these interstitial structures.

To calculate diffusion rates the concentration of vacancies is required (Equation 4). For intrinsic diffusion we have assumed this comes from minimising the free energy of the Frenkel reaction ($Mg_{Mg}^{X} \rightarrow V_{Mg}'' + Mg_{I}^{\bullet\bullet}$) (Dohmen and Chakraborty, 2007). When this reaction proceeds forward the positive enthalpy and the negative configurational entropy term both increase and at some concentration this provides a minimum energy. As the Mg vacancy and the Mg interstitial are each able to occupy two sites solving analytically for the free energy minimum is awkward. Instead we calculate the number of different arrangements of Mg vacancies and defects in the crystal considering all M1, M2, I1 and I2 sites and then calculate the probability of their occurrence and thus their configurational entropy. The steps for this are given in the supplementary information but the final

result is that the equilibrium concentration in the intrinsic case comes from minimising the free energy, given by:

$\Delta G = \Delta E \times a - TS_{confa}$ Equation 8

where *a* is a reaction vector for the Frenkel reaction (between 0 and 1), Δ*E* is the energy of the Frenkel reaction and S_{confa} is the configurational entropy after the reaction has proceeded forward by *a*. The results of this minimisation are given in Table 1. Pressure strongly decreases the number of defects (by increasing the positive formation internal energy U) that are formed thermodynamically whereas temperature increases the number of defects (as the configuration entropy is multiplied by -T).

We have assumed that the only relevant intrinsic defect reaction for Mg diffusion is the Mg Frenkel reaction. We can test this assumption by examining the energy of other potential intrinsic reactions that produce Mg defects to examine if they could compete energetically with the Mg Frenkel reaction. To do this we calculated the energy of the following reactions:

R1) $Mg_{Mg}^{X} \rightarrow V_{Mg}^{''} + Mg_{I}^{\bullet\bullet}$

R2) $Mg_{Mg}^{X} + O_{O}^{X} \rightarrow V_{Mg}^{''} + V_{O}^{\bullet\bullet} + MgO$

R3) $MgO \rightarrow Mg_{I}^{\bullet\bullet} + O_{I}^{''}$

R4) $2V_{Mg}^{''} + Si_{Si}^{X} + 4MgO \rightarrow V_{Si}^{''''} + 2Mg_{Mg}^{X} + Mg_2SiO_4$

R5) $Si_{Si}^{X} + 4MgO \rightarrow V_{Si}^{''''} + 2Mg_{I}^{\bullet\bullet} + Mg_2SiO_4$

R6) $Mg_2SiO_4 + Si_{Si}^{X} + 2Mg_{Mg}^{X} \rightarrow 2V_{Mg}^{''} + Si_{I}^{\bullet\bullet\bullet\bullet} + Si_{Si}^{X} + 4MgO$

In constructing these reactions we have assumed that the crystal remains charge neutral and thus all reactions are charge balanced. We have considered the most simple intrinsic reactions that produce a Mg vacancy or an Mg interstitial, more complex reactions that could be constructed by adding these reactions together are implicitly included. The Schottky defect which produces Mg, Si and O vacancies simultaneously is not included here because we predict that it has extremely high energy (>36 eV) and thus is very unlikely to occur as has also been found previously (Bejina et al., 2009, Walker et al., 2009).

The energy of these reactions (R1-R6) is shown in Table S2 but all other reactions have substantially higher energies than the Frenkel reaction (R1) and thus are considerably less favoured to occur. By calculating the free energy minimum of the above reactions we can calculate the equilibrium concentration of defects that occurs in pure forsterite. We did this with two frameworks- 1 where the only possible reaction is R1 and one where R1-R6 can all occur. By including the reactions R2-R6, which compete with R1 in configurational entropy space, we predict that the concentration of Mg defects changes by less than 0.001% when compared to the system with R1 alone. Thus alternative methods of intrinsic defect production do not significantly compete with the Mg Frenkel reaction R1 and can be safely ignored and from now on we shall only consider the Mg Frenkel reaction R1. It should be reemphasized that we are only considering pure forsterite and intrinsic defects in this work and extrinsic defects are likely to compete with R1. We shall consider the possible effect of extrinsic defects in the discussion section.

All reactions above have been written in an MgO buffered system- to consider an enstatite buffered system appropriate amounts of the reaction:

R7) $MgO+MgSiO_3 \rightarrow Mg_2SiO_4$

could be added to the system. In the pure forsterite system where only intrinsic defects are important we predict that Mg diffusion rates will be the same in MgO and $MgSiO_3$ buffered systems because R1 does not depend upon SiO_2 activity. Thus our results should apply in both of these systems.

Experimentally a difference in Mg diffusion rates has been seen between MgO and $MgSiO_3$ buffered systems (Jollands et al., 2020). This difference was explored in Muir et al. (2020) where it was predicted to arise due to interaction between extrinsic Al defects and $MgSiO_3$. This difference does not apply therefore in the intrinsic-only system in this paper but is important for comparisons to experimental data in real crystals. While there are many possible extrinsic defect+buffer reactions in real crystals, in Muir et al. (2020) experimental results from Jollands et al. (2020) were matched by considering the MgO-buffered case as purely intrinsic defects and the $MgSiO_3$ buffered case as

303 intrinsic+Al extrinsic defects. This suggests that, at least in these specific experiments and
304 compositions, the MgO-buffered experiments were closer to the pure intrinsic case and therefore we
305 shall compare our theoretical intrinsic results to MgO-buffered experiments to avoid any Al+$MgSiO_3$
306 effects.

307

308 *3.3 Vacancy Hops*

309 For Mg diffusion by vacancy hopping we found six different vacancy diffusion hops for which we
310 calculated the geometries and energies of hopping. The hops that we have considered are shown and
311 labelled in Figure 1 with their dimensions listed in Table S3 and described in the Supplementary
312 Information.

313 The activation energies and frequencies of these hops are presented in Table 2 and the barriers to
314 diffusion are shown in Figure 2. Notably the A hop which is directly along the [001] direction has a
315 substantially lower activation energy than all other M1 hops. The easiest hop from an M2 site is the
316 C hop back to an M1 site. These two effects combine such that vacancies will diffuse easily along the
317 [001] direction when in a M1 site and will have difficulty escaping to an M2 site. If they do escape to
318 an M2 site they will be converted quickly back to an M1 site. The weighted probability of these hops
319 is shown in Figure 2 (and an alternative representative in Figure S2) demonstrating the overwhelming
320 dominance of the A hop.

321 Comparing our activation energies to published values we find that our value for the favoured A hop
322 of 0.75 eV is similar to literature values of 0.72 (Walker et al., 2009) and 0.62 eV (Bejina et al., 2009).
323 Our other hops have some variation with those found in Walker et al. (2009)**.** To test whether this
324 was an effect of simply using DFT as against using forcefields we recalculated our results using GULP
325 with the TBH1 forcefield (Price et al., 1987, Sanders et al., 1984, Lewis and Catlow, 1985) (Table S4,
326 computational details in supplementary information). We find that generally DFT produces lower
327 barriers than forcefield calculations but that the order of the hops is the same. Crucially the activation
328 energy of the easiest A hop (which largely controls the overall diffusion) is very similar with both

methods (0.75 eV with DFT, 0.77 eV with our forcefield) which means that both DFT and forcefield calculations return a very similar diffusivity for vacancy diffusion.

We also considered the effect of pressure on the activation energies of these vacancies. As shown in Table S5 and Table S6 going from 0 to 10 GPa makes negligible differences to the activation energy or v^* of any of the hops. The effect of pressure on the vacancy concentration as described above is much more important.

3.4 Mg interstitial hops

As Mg interstitials occupy M1 and I2 sites – the latter of which are simply shifted M2 sites – the relative geometry of interstitial hops are identical to those of vacancies. These hops are pictured and labelled in Figure 3 and their barriers in Figure 4 (and tabulated in Table S7) with their energies and frequencies in Table 2 (and more pressures are listed in Table S6 and S8). The probability of any of the hops occurring is shown in Figure 4 and alternatively in Figure S3. These are again described in the supplementary information.

Interstitial hops I and J, which are between M1 and I2 sites, are the most favourable with activation energies <0.6 eV. In part this is because in the split M1 configuration one Mg at the M1 site is already close to an I2 site. Pressure has a small effect on the attempt frequency (Table S6) but a relatively large effect on the activation energy of these hops (Table S8) with hop I becoming nearly barrierless by 10 GPa. All vacancy hops and interstitial hops from the I2 site show similar attempt frequencies for hops with little geometry distortion (1×10^{-13} to 3×10^{-15} Hz) whereas interstitial hops from the I1 site show much lower attempt frequencies due to the large geometry distortions involved.

3.5 Diffusion

Using our KMC algorithm we can convert hops into diffusion rates. The diffusion coefficients for both vacancy and interstitial hopping are presented in Table 3 (these are listed at 5 and 10 GPa in Table S9 and S10). Vacancy diffusion is highly anisotropic with diffusion along [001] being orders of magnitude faster than diffusion along [100] or [010]. This is an outcome of the individual hop geometries where

355 the hop directly along [001] is ~0.75 eV easier than any other M1 hop. In the absence of any additional
356 undiscovered hops/mechanisms this will always hold. Interstitial diffusion is much more isotropic than
357 vacancy diffusion due to the favourability of M1 to I2 hops (I and J) which go in all three primary
358 directions.
359 To calculate total diffusion of Mg in forsterite we added together the rates of Mg vacancy and
360 interstitial diffusion. This assumes that Mg Frenkel pairs are not associated with each other. To test
361 this assumption, we calculated the binding energy of this pair by running separate simulations with
362 isolated Mg vacancies and interstitials and then calculations with them adjacent in the same unit cell
363 and comparing the difference in enthalpy. We find that the binding energy is approximately -1.9 eV
364 with a negative number indicating that bound defects are more stable than unbound defects. This is
365 a large number but it is much smaller than the configurational energy gains of randomly scattering Mg
366 vacancy and interstitial pairs for low concentrations. For the pairing energy to exceed this
367 configuration entropy, the defect concentration would need to be above 1.2×10^{-3} defects per unit cell
368 at 1300 K, many orders of magnitude larger than the predicted vacancy concentrations (Table 1). Thus
369 the Mg vacancy and interstitial pairs are unlikely to be associated with each other and can be modelled
370 individually here.
371 Figure 5 compares our pressure corrected (pressure is shifted by -3.95 GPa, see supplementary
372 information) results with some experimental measures of Mg self-diffusion at 0 GPa. We only plotted
373 results for experiments buffered with MgO because enstatite has been observed to increase Mg
374 diffusion rates by nearly 1 order of magnitude (Jollands et al., 2020) and thus involves more complex
375 effects as discussed above. For Chakraborty *et al.* 1994 we plotted the results without buffer as the
376 SiO_2 activity of these experiments is likely controlled by MgO (Jollands et al., 2020). In the [001]
377 direction our results are similar to those of Jollands *et al.* 2020. The absolute value of our results,
378 however, is somewhat unreliable as it is largely dependent on the choice of V_0^{exp} and thus the
379 pressure correction. This is shown in Figure S4 where a larger (-5 GPa) pressure correction was applied
380 and we find diffusion rates in the [001] direction very similar to those of Chakraborty *et al.* 1994. The

results presented in Figure 5 use what we consider the most reliable pressure correction. Regardless our calculated [001] diffusion lies in the experimental range. In the [100] and [010] direction our results are within the experimental scatter of Andersson et al. (1989) but not that of Jollands *et al.* 2020 and with the alternative correction our results lie within those of Chakraborty *et al.* 1994 for the [010] but not the [100] direction.

The experimental results and our theoretical results have some considerable differences from each other. While partly this is due to self-diffusion experiments being very difficult there is another possible cause. The most likely cause of these discrepancies is the presence of different extrinsic defects across different experimental samples. Different extrinsic defects, even if they do not diffuse themselves, could vary the N_{vac} and N_{Int} terms in Equation 4 and thus vary the diffusion rate. Such a variation would only have a very small effect on the experimentally determined activation energy unless the extrinsic defects were themselves produced thermally. Traditional measures of crystal purity are not adequate to accurately judge this effect as the key parameter is not so much the presence of different extrinsic defects but how these defects affect the intrinsic defects on a sub ppb level. Our model only considers intrinsic defects and thus will always be expected to have some difference with real crystals. To fully address this a large thermodynamic model needs to be built which is beyond the scope of this work but different experiments and our results are all within an order of magnitude of each other suggesting that primarily Mg diffusion in forsterite operates through intrinsic defects with extrinsic defects only leading to mild secondary effects.

Our ability to replicate the results of Jollands et al. (2020) suggests that our model for diffusion in forsterite accurately captures the situation in these experiments. Critically if interstitials are not included in our model while [001] diffusion can be modelled accurately, [100] and [010] diffusion would be orders of magnitude slower than has been observed in any experiment.

We next consider the effect of pressure. Figure 6 shows our [001] diffusion rates (with values listed in Table S11) as a function of pressure. Notably we find a larger pressure derivative for intrinsic

diffusion coefficients than has been seen in the literature (Chakraborty et al., 1994, Fei et al., 2018). Our activation volumes are 6.69 cm^3/mol at 1000 K, 7.51 cm^3/mol at 1300 K and 7.84 cm^3/mol at 1600 K. The pressure dependence of diffusion is strongly controlled in our calculations by the pressure dependence of defect concentration (Table 1) with little effect of the defect mobility (Table 3). Small changes to the formation energy of the Frenkel defect can have a strong effect on this dependence. If the number of defects is held constant across pressure then the calculated activation volumes are much smaller, ranging from -0.30 to 0.15 cm^3/mol. These lower activation volumes are of relevance for cases where pressure does not alter the number of vacancies. For example, in an extrinsic regime (where vacancies form to charge balance impurities) the vacancy concentration is not temperature or pressure dependent and only the direct effect of pressure on vacancy mobility is important. In a real crystal with few impurities there will be a balance between the number of vacancies formed intrinsically via Frenkel pairs and the number of vacancies associated with impurities. In such a case, the effective activation volume will fall between our high and low values as is observed experimentally. This will also be the case when the pressure upon a crystal is modified during an experiment but the crystal is not given time to reequilibrate its defect concentration.

With increasing extrinsic vacancies the anisotropy of diffusion also likely increases as discussed below. Thus we predict that a decreasing activation volume of diffusion (going from our high range to our low range) should be linked to an increasing anisotropy of diffusion (with [001] being the fast direction). A test of our predictions would be whether these 2 measurable parameters are actually interlinked.

4. Discussion

4.1 Anisotropic intrinsic diffusion

One of the most notable features of our results is that Mg diffusion can be strongly anisotropic. Figure 7 shows the anisotropy of Mg diffusion as a function of pressure. We find that anisotropy decreases with pressure due to the increasing importance of interstitial diffusion, which is less anisotropic, while temperature has little effect on anisotropy. At 1600 K and 0 GPa (corrected) we find the ratio of

diffusion in different directions [001]:[100] to be ~15 and [001]:[010] to ~6. Experimental measures of these ratios yield lower anisotropy with [001]:[100] having values of ~3 (Chakraborty et al., 1994), 3.5-7 (Jollands et al., 2020) and 7-40 (Andersson, 1987), and [001]:[010] having values of 4.5 (Chakraborty et al., 1994), 1.5-3.5 (Jollands et al., 2020) and 5-13 (Andersson, 1987). These experimental measurements were all at ambient pressure. Our calculated values for diffusional anisotropy are somewhat larger than has been seen experimentally. Our pressure correction method has not been calibrated for defect production and mobility and if the pressure correction was somewhat larger our anisotropies would approach the experimental range. One possible way to reduce the anisotropy would be to increase the ratio of Mg interstitials to Mg vacancies which could occur in the presence of extrinsic sources of Mg interstitials or impurities that fill Mg vacancies. Alternatively, there could be some macroscopic effect (e.g. from grain boundaries or dislocations) that reduces diffusional anisotropy in real crystals that we do not model.

Another issue is the order of diffusion rates in the different directions. Our calculations and some experiments (Andersson et al., 1989, Jollands et al., 2020) predict diffusion rates to be ordered [001]>[010]>[100] while Chakraborty et al. (1994) measured diffusion rates to be [001]>[100]>[010]. We do not have a source for this discrepancy as in our model both [010] and [100] diffusion are almost entirely controlled by interstitial I and J hops and thus their relative rate is fixed by the geometry of the crystal and not by any variable parameter. Temperature has an effect on the ratio of [100]:[010] diffusion but, as shown in Figure 7, this is small and [010] diffusion is predicted to be always faster than [100] diffusion. We have no hops that could selectively increase the [100] diffusion rate that are even close to being viable. Thus the presence of evidence suggesting that diffusion along [100] can sometimes be faster than diffusion along [010] suggests some kind of atomistic or macroscopic effect that is not being modelled in our system.

4.2 Anisotropy Changes in the Upper Mantle

While the dependence of anisotropy on pressure is large this probably has little importance in the upper mantle. After applying pressure corrections a 0-10 GPa range in the upper mantle would be equivalent to ~4-16 GPa in our pressure scales. The largest changes in anisotropy come at the lowest pressures and so across the pressure range of the upper mantle, changes in Mg diffusional anisotropy with depth will typically be up to an order of magnitude except at the coldest temperatures (1000 K) where this could reach 1.5 orders of magnitude. These changes are likely to be too small to have any major effects on mantle rheology that change with depth except at the very top of the upper mantle where temperatures are low.

4.3 The effect of extrinsic vacancies

Other substances such as iron (Chakraborty, 2010, Dohmen et al., 2007, Dohmen and Chakraborty, 2007) or water (Fei et al., 2018) that are in olivine can substantially change the diffusion rate. Without substantial changes to the diffusion mechanism there are two ways this can happen 1) through modifying the concentration of defects (N_{Vac}, N_{Int}) or 2) through modifying the mobility (D_{Mg}^{Vac}, D_{Mg}^{Int}) of defects. All substances that modify the diffusion rate likely do the former while only some do the latter. Iron can increase the number of Mg vacancies through the following reaction (Dohmen and Chakraborty, 2007, Chakraborty, 2010):

R8) $6Fe_{Mg}^{X} + SiO_2 + O_2(g) \rightarrow 2V_{Mg}'' + 4Fe_{Mg}^{\bullet} + Fe_2SiO_4$

whereas water can produce $(2H)_{Mg}^{X}$ vacancies. R8 has been invoked as the controlling reaction in Mg diffusion at intermediate temperatures in what is known as the Transition Metal Extrinsic Domain (TAMED) (Chakraborty, 2010). In the Fe-Mg interdiffusion case the mobility of vacancies is also modified as they include Fe self-diffusion coefficients. In this and other cases we expect the change in the concentrations of vacancies to generally outweigh the changes to the mobility of vacancies due to the small number of intrinsic defects produced by the Frenkel reaction. Extrinsic Mg vacancy concentrations can be many orders of magnitude higher than our predicted intrinsic Mg vacancy concentration in many systems. Thus the prime reason that various contaminants cause an increase

in Mg diffusion rates is likely to be the production of more Mg vacancies. Critically Mg vacancies can be produced in this way but producing extrinsic Mg interstitials is much more difficult. This means that extrinsic defects are likely to produce a strong imbalance in the Mg vacancy vs Mg interstitial ratio.

Producing Mg vacancies in excess of Mg interstitials would cause strong changes to the anisotropy of diffusion. This effect is explored in Figure 8 where we plot how increasing the diffusion rate solely by adding Mg vacancies changes the anisotropy of diffusion. We are not aware of any studies on diffusional anisotropy in forsterite with large amounts of defects so instead we use our model to predict the anisotropy from the measured diffusion rates. We do this by assuming two things: 1) any change in Mg diffusion rate from the Mg self diffusion rate (D_{sd}) in Equation 4 is due to extrinsic Mg vacancies and 2) that extrinsic Mg vacancies do not bind to any charge balancing impurities that produce them (D_{Mg}^{Vac} is identical for intrinsic and extrinsic Mg vacancies). Then we use Equation 9:

$$D_x = D_{sd} + D_{Mg}^{Vac} N_{Vacex} \quad \text{Equation 9}$$

where D_x is the target diffusion rate, D_{sd} is determined from Equation 4 and N_{vacex} is the concentration of extrinsic Mg vacancies that is varied until D_x matches the desired value. Using this framework we explore the effects of two defective elements Fe (1-20%) (Dohmen and Chakraborty (2017) and water (1-100 ppm) (Fei *et al.* 2018). At 1300 K we predict these defects to increase diffusional anisotropy (compared to perfect forsterite) by 2-5 times at 5-10 GPa (uncorrected). As temperature increases this effect decreases such that by 1600 K iron and water increase diffusional anisotropy by less than 1.2 times. Thus at the high pressures and temperatures of the upper mantle the measured experimental diffusion rates of both water and iron containing forsterite can be matched by adding in extrinsic Mg defects without large increases in diffusional anisotropy. Thus for these compositional ranges we do not expect extrinsic vacancies to lead to significant anisotropy for Mg diffusion in the upper mantle. With larger increases in the Mg diffusion rate through larger concentrations of extrinsic defects or at colder temperatures we do predict that there will be a large increase in diffusional anisotropy and that this increase will be accompanied by a decrease in activation volume of diffusion.

Thus we predict that diffusion rate, diffusion anisotropy and activation volume of diffusion are all correlated to the concentration of extrinsic vacancies.

Conclusions

We find that the anisotropy of Mg diffusion in forsterite is heavily dependent upon conditions with pressure strongly decreasing the anisotropy while temperature only weakly affects it. In the presence of extrinsic vacancies temperature strongly controls diffusional anisotropy with samples at low temperatures having potentially extremely high diffusional anisotropy (>500 times faster in the [001] direction). This has strong implications for diffusion chronometry and conductivity (and other properties dependant on Mg diffusion rates) which need to include corrections for pressure, temperature and impurity content alongside orientation to account for this effect.

In this work we outline a simple atomistic model which is able to replicate measured experimental diffusion rates along the [001] direction. We find that to explain experimental diffusion rates in the [100] and [010] directions interstitial diffusion is required alongside vacancy diffusion.

The next step is to consider how other components could affect this diffusion such as is shown by our simple extrinsic vacancy model in Figure 8. Additional components can either affect the number and balance of Mg vacancies and interstitials or they can affect the intrinsic diffusion of Mg vacancies and interstitials. The former effect can be considered by examining the energetics of defect forming reactions and how contaminants change these energetics- particularly through changing the configurational entropy balances- and the latter can be considered for contaminants that directly change Mg vacancies or interstitials by interacting with them.

Acknowledgments

Funding was provided by National Natural Science Foundation of China (41773057, 42050410319), and by the National Environment Research Council as part of the Volatiles, Geodynamics and Solid Earth Controls on the Habitable Planet research programme (NE/M000044/1). JM is highly thankful to Chinese Academy of Sciences (CAS) for PIFI.

Bibliography

AMMANN, M. W., BRODHOLT, J. P., WOOKEY, J. & DOBSON, D. P. 2010. First-principles constraints on diffusion in lower-mantle minerals and a weak D '' layer. *Nature,* 465**,** 462-465.

ANDERSSON, K. 1987. *Materietransport und Defektstrukturen in kristallinem Magnesiumorthosilicat bei höheren TemPeraturen.* Technischen Universität Clausthal.

ANDERSSON, K., BORCHARDT, G., SCHERRER, S. & WEBER, S. 1989. Self-diffusion in Mg_2SiO_4 (forsterite) at high temperature. *Fresenius Zeitschrift Fur Analytische Chemie,* 333**,** 383-385.

BAGATUR'YANTS, A. A., KORKIN, A. A., NOVOSELOV, K. P., SAVCHENKO, L. L. & UMANSKII, S. Y. 2003. Integrated approach to atomistic simulation of film deposition processes. *In:* CATLOW, C. R. A. & KOTOMIN, E. A. (eds.) *Computational Materials Science.* USA: IOS Press.

BEJINA, F., BLANCHARD, M., WRIGHT, K. & PRICE, G. D. 2009. A computer simulation study of the effect of pressure on Mg diffusion in forsterite. *Physics of the Earth and Planetary Interiors,* 172**,** 13-19.

BORTZ, A. B., KALOS, M. H. & LEBOWITZ, J. L. 1975. NEW ALGORITHM FOR MONTE-CARLO SIMULATION OF ISING SPIN SYSTEMS. *Journal of Computational Physics,* 17**,** 10-18.

BRAITHWAITE, J. S., WRIGHT, K. & CATLOW, C. R. A. 2003. A theoretical study of the energetics and IR frequencies of hydroxyl defects in forsterite. *Journal of Geophysical Research-Solid Earth,* 108.

BRODHOLT, J. 1997. Ab initio calculations on point defects in forsterite (Mg2SiO4) and implications for diffusion and creep. *American Mineralogist,* 82**,** 1049-1053.

BULATOV, V. V. & CAI, W. 2006. *Computer Simulations of Dislocations,* UK, Oxford University Press.

CHAKRABORTY, S. 2010. Diffusion Coefficients in Olivine, Wadsleyite and Ringwoodite. *In:* ZHANG, Y. X. & CHERNIAK, D. J. (eds.) *Diffusion in Minerals and Melts.*

CHAKRABORTY, S., FARVER, J. R., YUND, R. A. & RUBIE, D. C. 1994. MG TRACER DIFFUSION IN SYNTHETIC FORSTERITE AND SAN-CARLOS OLIVINE AS A FUNCTION OF P, T AND FO2. *Physics and Chemistry of Minerals,* 21**,** 489-500.

CLARK, S. J., SEGALL, M. D., PICKARD, C. J., HASNIP, P. J., PROBERT, M. J., REFSON, K. & PAYNE, M. C. 2005. First principles methods using CASTEP. *Zeitschrift fuer Kristallographie,* 220**,** 567-570.

DOHMEN, R., BECKER, H.-W. & CHAKRABORTY, S. 2007. Fe-Mg diffusion in olivine I: experimental determination between 700 and 1,200 degrees C as a function of composition, crystal orientation and oxygen fugacity. *Physics and Chemistry of Minerals,* 34**,** 389-407.

DOHMEN, R. & CHAKRABORTY, S. 2007. Fe-Mg diffusion in olivine II: point defect chemistry, change of diffusion mechanisms and a model for calculation of diffusion coefficients in natural olivine. *Physics and Chemistry of Minerals,* 34**,** 409-430.

FEI, H. Z., KOIZUMI, S., SAKAMOTO, N., HASHIGUCHI, M., YURIMOTO, H., MARQUARDT, K., MIYAJIMA, N. & KATSURA, T. 2018. Mg lattice diffusion in iron-free olivine and implications to conductivity anomaly in the oceanic asthenosphere. *Earth and Planetary Science Letters,* 484**,** 204-212.

HARTLEY, M. E., MORGAN, D. J., MACLENNAN, J., EDMONDS, M. & THORDARSON, T. 2016. Tracking timescales of short-term precursors to large basaltic fissure eruptions through Fe-Mg diffusion in olivine. *Earth and Planetary Science Letters,* 439**,** 58-70.

JAOUL, O. 1990. MULTICOMPONENT DIFFUSION AND CREEP IN OLIVINE. *Journal of Geophysical Research-Solid Earth and Planets,* 95**,** 17631-17642.

JAOUL, O., BERTRANALVAREZ, Y., LIEBERMANN, R. C. & PRICE, G. D. 1995. FE-MG INTERDIFFUSION IN OLIVINE UP TO 9 GPA AT T=600-900-DEGREES-C - EXPERIMENTAL-DATA AND COMPARISON WITH DEFECT CALCULATIONS. *Physics of the Earth and Planetary Interiors,* 89**,** 199-218.

JOLLANDS, M. C., ZHUKOVA, I. A., O'NEILL, H. S. & HERMANN, J. 2020. Mg diffusion in forsterite from 1250-1600 °C. *American Mineralogist***,** DOI: 10.2138/am-2020-7286.

KARATO, S., JUNG, H., KATAYAMA, I. & SKEMER, P. 2008. Geodynamic significance of seismic anisotropy of the upper mantle: New insights from laboratory studies. *Annual Review of Earth and Planetary Sciences.*

LEETMAA, M. & SKORODUMOVA, N. V. 2015. Mean square displacements with error estimates from non-equidistant time-step kinetic Monte Carlo simulations. *Computer Physics Communications,* 191**,** 119-124.

LEWIS, G. V. & CATLOW, C. R. A. 1985. POTENTIAL MODELS FOR IONIC OXIDES. *Journal of Physics C-Solid State Physics,* 18**,** 1149-1161.

MORIOKA, M. 1981. CATION DIFFUSION IN OLIVINE .2. NI-MG, MN-MG, MG AND CA. *Geochimica Et Cosmochimica Acta,* 45**,** 1573-1580.

MUIR, J. M. R., JOLLANDS, M., ZHANG, F. W. & WALKER, A. M. 2020. Explaining the dependence of M-site diffusion in forsterite on silica activity: a density functional theory approach. *Physics and Chemistry of Minerals,* 47.

OZAWA, K. 1984. OLIVINE-SPINEL GEOSPEEDOMETRY - ANALYSIS OF DIFFUSION-CONTROLLED MG-FE-2+ EXCHANGE. *Geochimica Et Cosmochimica Acta,* 48**,** 2597-2611.

PANKHURST, M. J., MORGAN, D. J., THORDARSON, T. & LOUGHLIN, S. C. 2018. Magmatic crystal records in time, space, and process, causatively linked with volcanic unrest. *Earth and Planetary Science Letters,* 493**,** 231-241.

POIRIER, J. P. 1985. *Creep in Crystals,* UK, Cambridge University Press.

PRICE, G. D., PARKER, S. C. & LESLIE, M. 1987. THE LATTICE-DYNAMICS OF FORSTERITE. *Mineralogical Magazine,* 51**,** 157-170.

SANDERS, M. J., LESLIE, M. & CATLOW, C. R. A. 1984. INTERATOMIC POTENTIALS FOR SIO2. *Journal of the Chemical Society-Chemical Communications***,** 1271-1273.

SCHOCK, R. N., DUBA, A. G. & SHANKLAND, T. J. 1989. ELECTRICAL-CONDUCTION IN OLIVINE. *Journal of Geophysical Research-Solid Earth and Planets,* 94**,** 5829-5839.

TENG, F. Z., DAUPHAS, N., HELZ, R. T., GAO, S. & HUANG, S. C. 2011. Diffusion-driven magnesium and iron isotope fractionation in Hawaiian olivine. *Earth and Planetary Science Letters,* 308**,** 317-324.

TILLEY, R. J. D. 1987. *Defect Crystal chemistry and its applications,* United States, Kluwer Academic Publishers.

VINEYARD, G. H. 1957. FREQUENCY FACTORS AND ISOTOPE EFFECTS IN SOLID STATE RATE PROCESSES. *Journal of Physics and Chemistry of Solids,* 3**,** 121-127.

VOCADLO, L., WALL, A., PARKER, S. C. & PRICE, G. D. 1995. ABSOLUTE IONIC-DIFFUSION IN MGO - COMPUTER CALCULATIONS VIA LATTICE-DYNAMICS. *Physics of the Earth and Planetary Interiors,* 88**,** 193-210.

VOTER, A. F. 2007. INTRODUCTION TO THE KINETIC MONTE CARLO METHOD. *In:* SICKAFUS, K. E., KOTOMIN, E. A. & UBERUAGA, B. P. (eds.) *Radiation Effects in Solids.* Dordrecht: Springer.

WALKER, A. M., WOODLEY, S. M., SLATER, B. & WRIGHT, K. 2009. A computational study of magnesium point defects and diffusion in forsterite. *Physics of the Earth and Planetary Interiors,* 172**,** 20-27.

WRIGHT, K. & CATLOW, C. R. A. 1994. A computer simulation study of (OH) defects in olivine. *Physics and Chemistry of Minerals,* 20**,** 515-518.

YOSHINO, T., MATSUZAKI, T., SHATSKIY, A. & KATSURA, T. 2009. The effect of water on the electrical conductivity of olivine aggregates and its implications for the electrical structure of the upper mantle. *Earth and Planetary Science Letters,* 288**,** 291-300.

YOSHINO, T., ZHANG, B. H., RHYMER, B., ZHAO, C. C. & FEI, H. Z. 2017. Pressure dependence of electrical conductivity in forsterite. *Journal of Geophysical Research-Solid Earth,* 122**,** 158-171.

Figure 1: Diagram of possible vacancy hops between M1 and M2 sites. The absolute distances of these hops are listed in Table S3. Mg atoms are brown, Si atoms are blue with their tetrahedrons highlighted, oxygen atoms are red.

Figure 2: Plot of the activation energy barriers to Mg vacancy hopping in forsterite. The energy of a vacancy is plotted at M1 (blue) (defined as 0 eV) and M2 (green) sites and at 7 points in-between each site with both the site and the intermediate points plotted with the same relative energy bar as shown. Many more intermediate points were used to determine the activation energy maximum than are shown here (see text for details). Hops in the [100] direction (hops B and F) are not shown but both of these hops have activation energies higher than all the hops pictured here. The black box represents a forsterite unit cell. For a sample M1 and an M2 site we have shown the main hops with a percentage likelihood of selecting this hop that was determined at 1300 K and 0 GPa (uncorrected).

Figure 3: Diagram of interstitial hops between M1 and I2 sites. The absolute distances of these hops are listed in Table S7. Octahedral holes are green.

Figure 4: As Figure 2 but for interstitial hops between M1 and I2 sites with the M1 sites being defined as 0 eV. The layer closer to the bottom of the graph are M1 and then I2 and M1 layers alternate going up the page. These sites are much closer in energy than the M1 and M2 sites for vacancy migration. Again hops along the [100] axis (H and L) are not shown but are very high in energy. With this projection I and I* and J and J* hops are on top of each other (as they are only varied along the [100] direction) but we have pictured the lower energy paths (I and J respectively).

Figure 5: Plot of experimental Mg self diffusion rates in MgO-buffered forsterite at 0 GPa alongside our predicted rates at 0 GPa (corrected- see supplementary information) determined by fitting between our pressure corrected values (the same plot with a 5 GPa pressure correction is shown in Fig S4). Rates have been separated by diffusion direction (colour- red= [001], green= [010], blue= [100]) and by the work they come from (symbol-see below). The lines represent our own calculations. In this collection we have excluded work in olivine and work buffered by enstatite. The mark for Fei *et al.* (2018a) was determined by our own extrapolation of the high temperature data across different pressures, all other points were as measured in the experiment. References are Morioka *et al.* 1981 triangles, Jollands *et al.* 2020 squares, Chakraborty *et al.* 1994 circles, Fei *et al.* (2018a) cross, Andersson *et al.* 1987 diamonds.

Figure 6: [001] Mg diffusion rates in perfect forsterite as a function of pressure at fixed temperatures (blue=1000 K, green=1300 K, red=1600 K) compared to results from Chakraborty *et al.* (1994) and Fei *et al.* (2018a). Model predictions are uncorrected (solid line) or pressure corrected (dotted line). For experimental data, data points are plotted and then a line is constructed using activation volumes of 1.1 cm^3/mol for Fei *et al.* (1994) and 4.3 cm^3/mol for Fei *et al.* (2018a). The results from Chakraborty *et al.* (1994) are those with no buffer with an f_{O_2} of 10^{-12}. In that paper a higher activation volume

(~3.4) was determined in air. The oxygen fugacity of Fei *et al.* (2018a) is unknown due to the complicating presence of water.

Figure 7: Log of the ratios of C/A ([001]/[100]) (dotted lines, circles) and C/B ([001]/[010]) Mg diffusion (solid line, squares) in perfect olivine as a function of pressure at different temperatures (blue 1000 K, green 1300 K, red 1600 K). Two pressure scales are shown, the pressure scale from DFT directly and one that has been corrected as per the text.

Figure 8: Comparision of anisotropy (defined as diffusion in the [001] direction/ diffusion in the [110] direction) for different diffusion rates (D_x) in a system of self diffusion+extrinsic vacancies. Anistropy is relative to pure forsterite which is 1. This was determined by solving Equation 9 as a function of diffusion rate. Lines are at 1000 K (blue), 1300 K (orange) and 1600 K and solid lines represent 5 GPa, dotted lines 10 GPa (uncorrected) which correct to around 1 and 6 GPa respectively.

The dark region represent the range of D_x between Fe=1-20% for olivine at 0 GPa, 1300 K and $fO^2=10^{-7}$ Dohmen and Chakraborty (2017). The light region represents the range of D_x for water ranging between 1-150 wt. ppm at ~8 GPA and 1300 K (Fei *et al.* 2018).

Table 1: Free energy of the Frenkel reaction at various pressures and temperatures and the corresponding concentration of vacancies and interstitials (in defects/unit cell) in a pure forsterite crystal where only the Mg Frenkel reaction forms significant defects- this concentration is for each defect type so the concentration of total defects (vacancies+interstitials) is twice this number.

Table 2: Activation energy and modified attempt frequency v* of various hops (shown in Figure 1 and 3 with the hop distances outlined in Table S4 and S8) for forsterite at 0 GPa uncorrected. Hop L could not be stabilised but is very high in energy. Hops with an asterisk go in the reverse direction where this is not equivalent.

Table 3: Diffusion coefficients (m^2/s) of vacancies and interstitials in three directions at 0 GPa (uncorrected) with 5 and 10 GPa (uncorrected) [001] diffusion coefficients also listed. For the other coefficients in [100] and [010] at 5 and 10 GPa see Table S10 and S11.

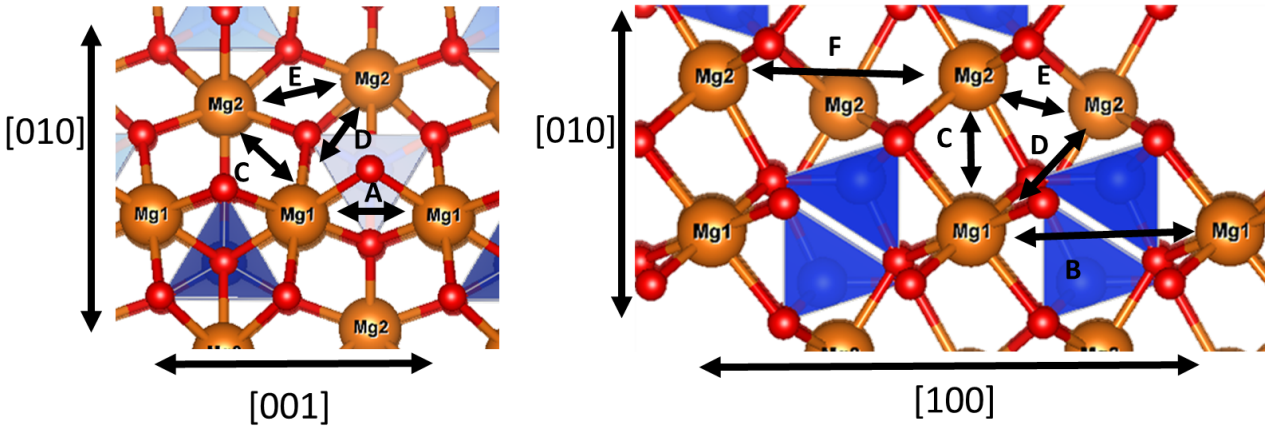

711

712 Figure 1:

713 Diagram of possible vacancy hops between M1 and M2 sites. The absolute distances of these hops
714 are listed in Table S3. Mg atoms are brown, Si atoms are blue with their tetrahedrons highlighted,
715 oxygen atoms are red.

716

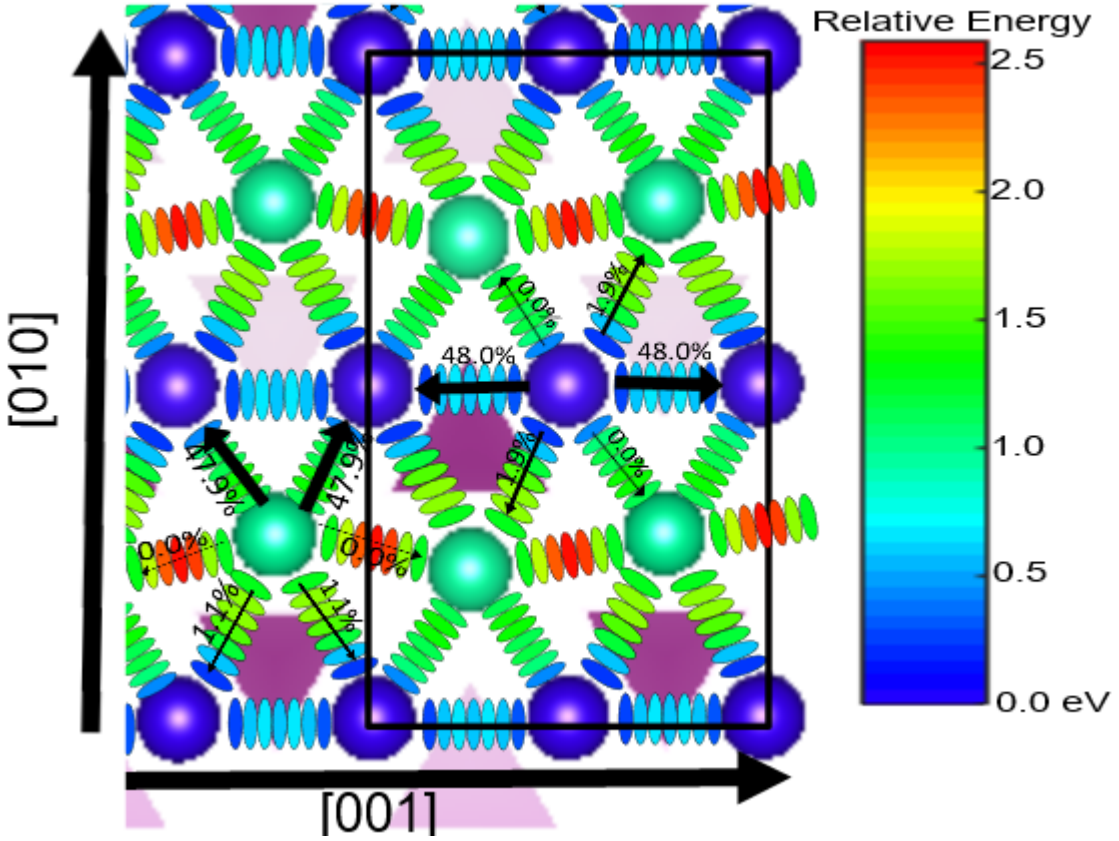

Figure 2: Plot of the activation energy barriers to Mg vacancy hopping in forsterite. The energy of a vacancy is plotted at M1 (blue) (defined as 0 eV) and M2 (green) sites and at 7 points in-between each site with both the site and the intermediate points plotted with the same relative energy bar as shown. Many more intermediate points were used to determine the activation energy maximum than are shown here(see text for details). Hops in the [100] direction (hops B and F) are not shown but both of these hops have activation energies higher than all the hops pictured here. The black box represents a forsterite unit cell. For a sample M1 and an M2 site we have shown the main hops with a percentage likelihood of selecting this hop that was determined at 1300 K and 0 GPa (uncorrected).

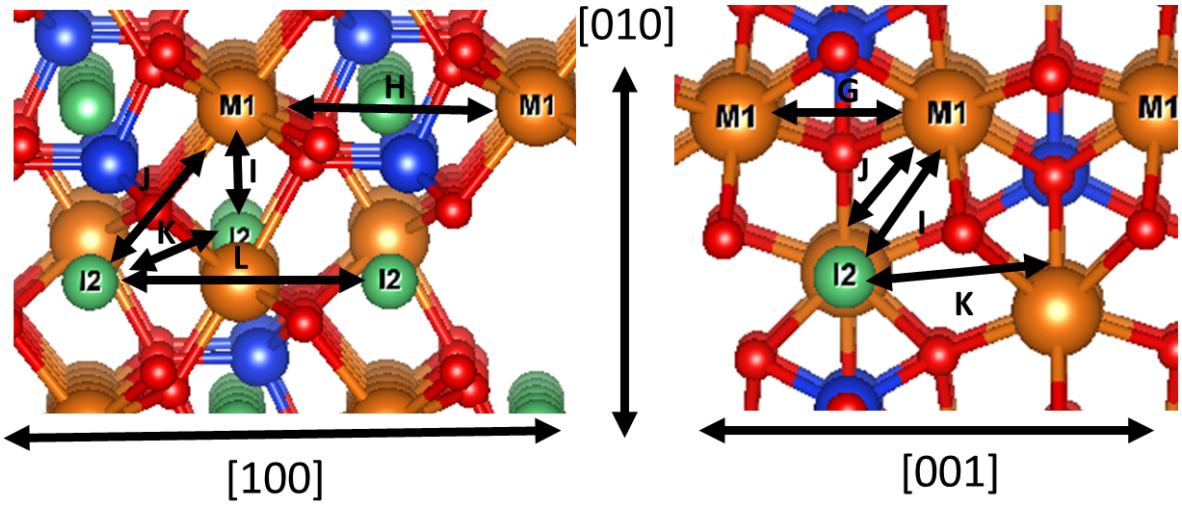

729

730 Figure 3:

731 Diagram of interstitial hops between M1 and I2 sites. The absolute distances of these hops are
732 listed in Table S7. Octahedral holes are green.

733

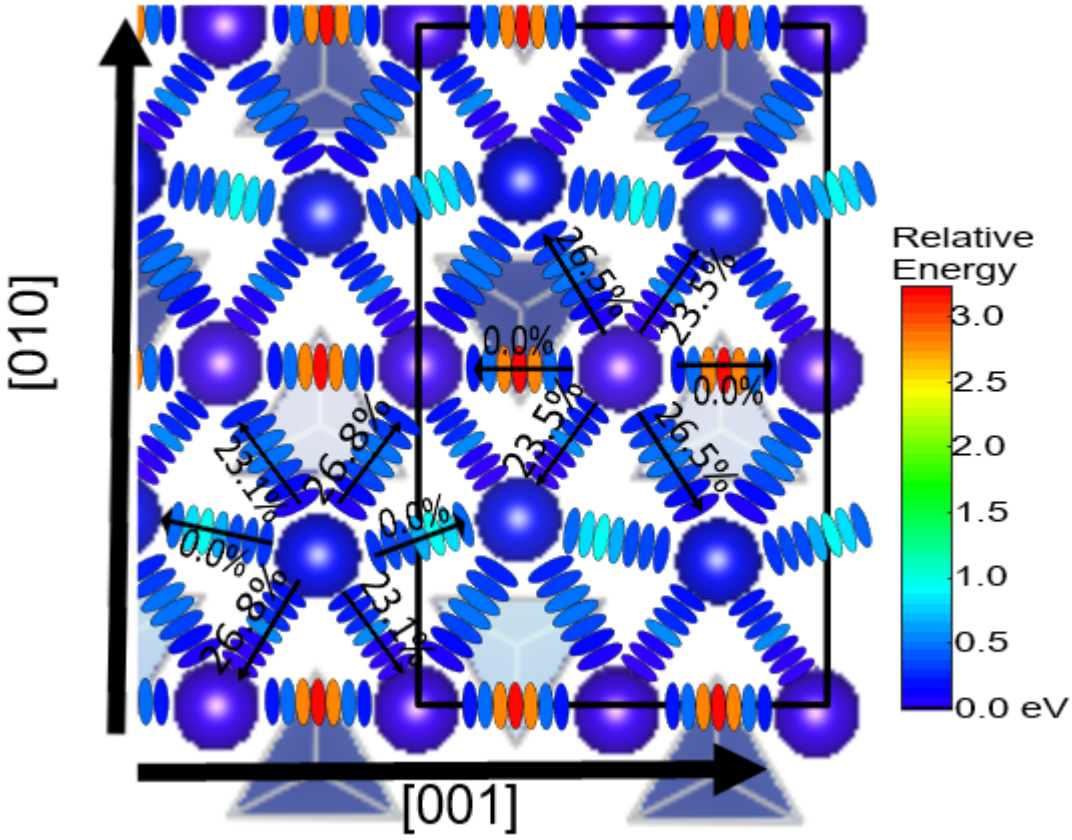

734

735 Figure 4: As Figure 2 but for interstitial hops between M1 and I2 sites with the M1 sites being
736 defined as 0 eV. The layer closer to the bottom of the graph are M1 and then I2 and M1 layers
737 alternate going up the page. These sites are much closer in energy than the M1 and M2 sites for
738 vacancy migration. Again hops along the [100] axis (H and L) are not shown but are very high in
739 energy. With this projection I and I* and J and J* hops are on top of each other (as they are only
740 varied along the [100] direction) but we have pictured the lower energy paths (I and J respectively).

741

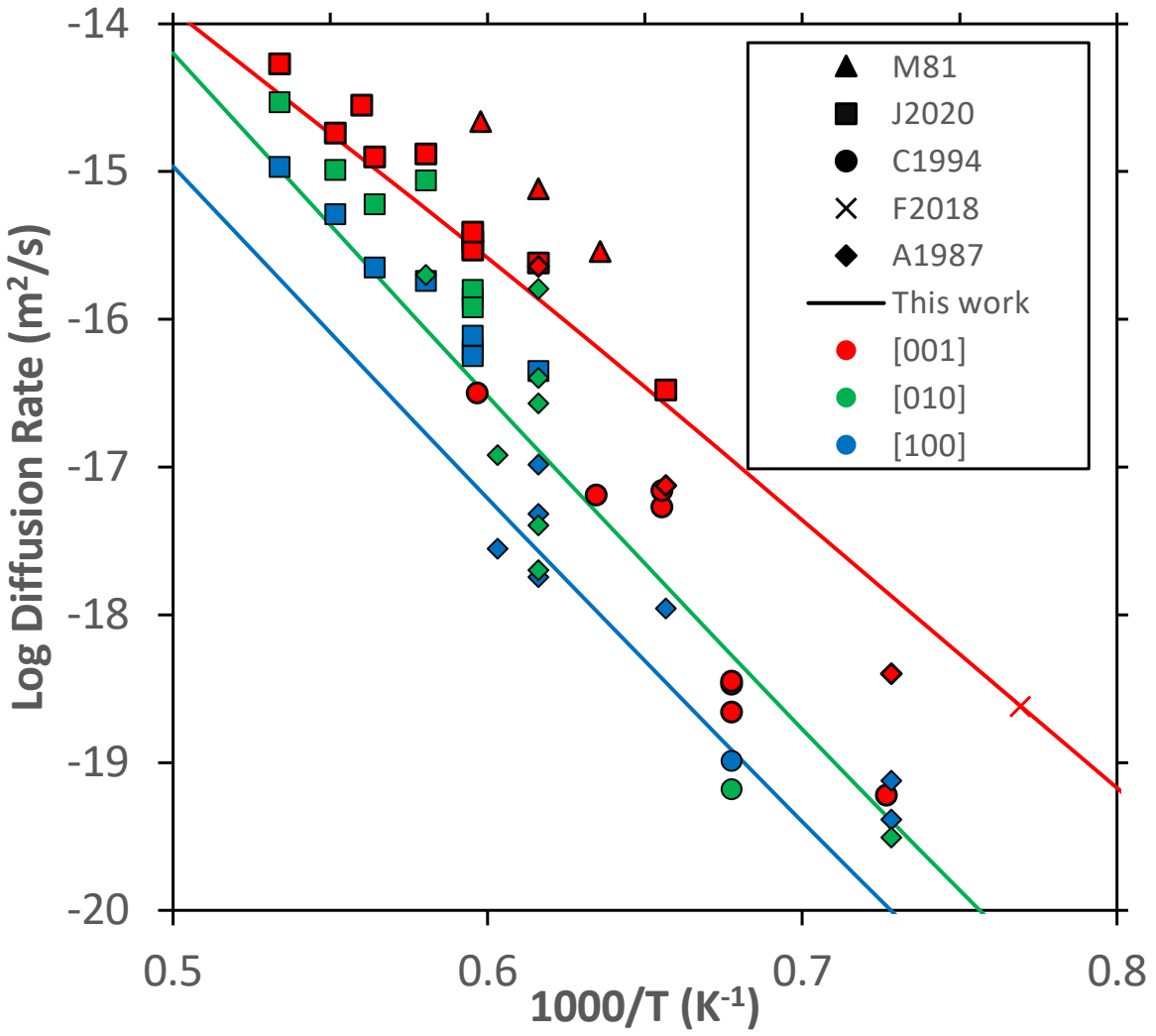

Fig 5: Plot of experimental Mg self diffusion rates in MgO-buffered forsterite at 0 GPa alongside our predicted rates at 0 GPa (corrected- see supplementary information) determined by fitting between our pressure corrected values (the same plot with a 5 GPa pressure correction is shown in Fig S4). Rates have been separated by diffusion direction (colour- red= [001], green= [010], blue= [100]) and by the work they come from (symbol-see below). The lines represent our own calculations. In this collection we have excluded work in olivine and work buffered by enstatite. The mark for Fei *et al.* (2018a) was determined by our own extrapolation of the high temperature data across different pressures, all other points were as measured in the experiment. References are Morioka *et al.* 1981 triangles, Jollands *et al.* 2020 squares, Chakraborty *et al.* 1994 circles, Fei *et al.* (2018a) cross, Andersson *et al.* 1987 diamonds.

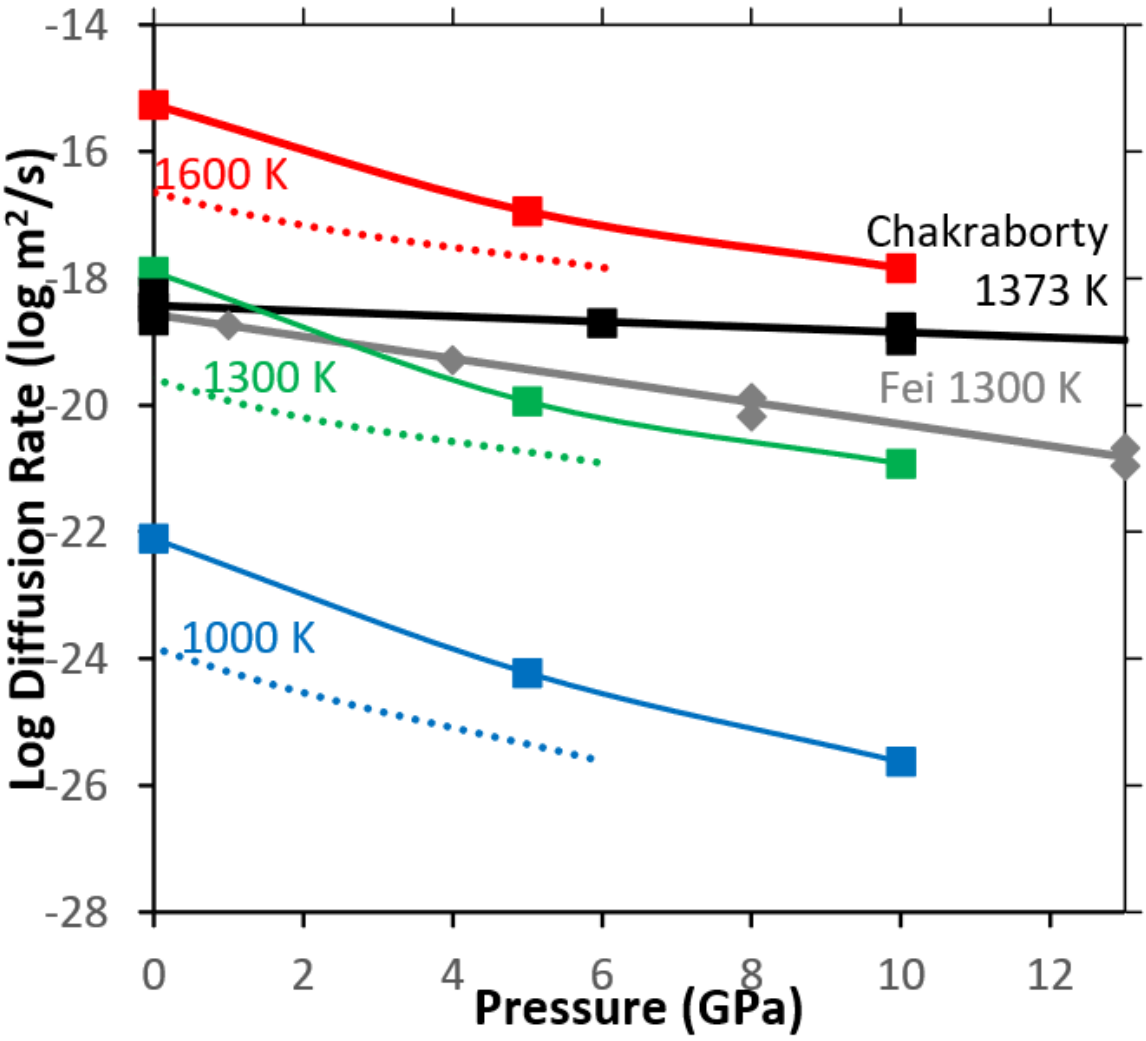

Figure 6: [001] Mg diffusion rates in perfect forsterite as a function of pressure at fixed temperatures (blue=1000 K, green=1300 K, red=1600 K) compared to results from Chakraborty *et al.* (1994) and Fei *et al.* (2018a). Model predictions are uncorrected (solid line) or pressure corrected (dotted line). For experimental data, data points are plotted and then a line is constructed using activation volumes of 1.1 cm^3/mol for Fei *et al.* (1994) and 4.3 cm^3/mol for Fei *et al.* (2018a). The results from Chakraborty *et al.* (1994) are those with no buffer with an f_{O_2} of 10^{-12}. In that paper a higher activation volume (~3.4) was determined in air. The oxygen fugacity of Fei *et al.* (2018a) is unknown due to the complicating presence of water.

768

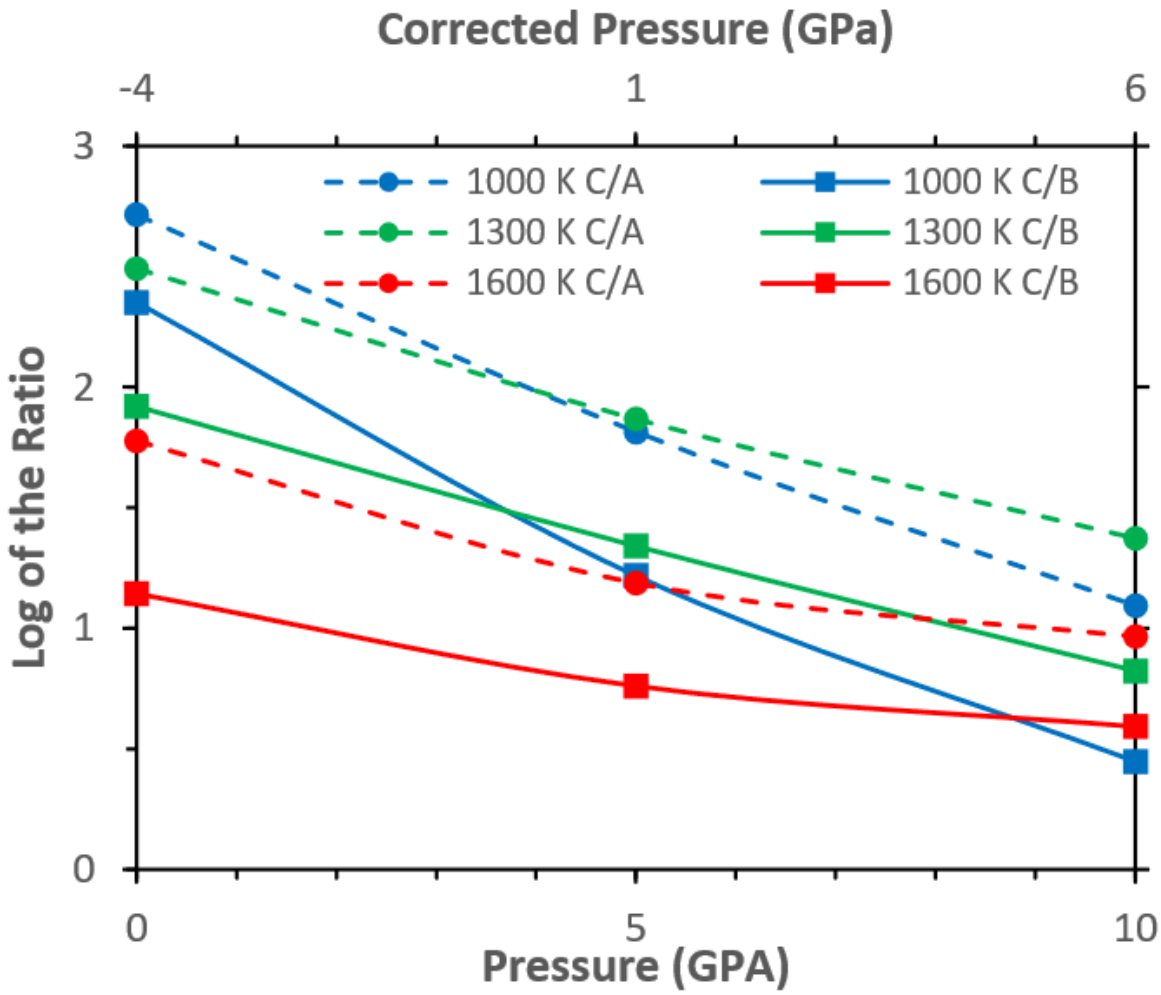

769

770 Figure 7: Log of the ratios of C/A ([001]/[100]) (dotted lines, circles) and C/B ([001]/[010]) Mg
771 diffusion (solid line, squares) in perfect olivine as a function of pressure at different temperatures
772 (blue 1000 K, green 1300 K, red 1600 K). Two pressure scales are shown, the pressure scale from
773 DFT directly and one that has been corrected as per the text.

774

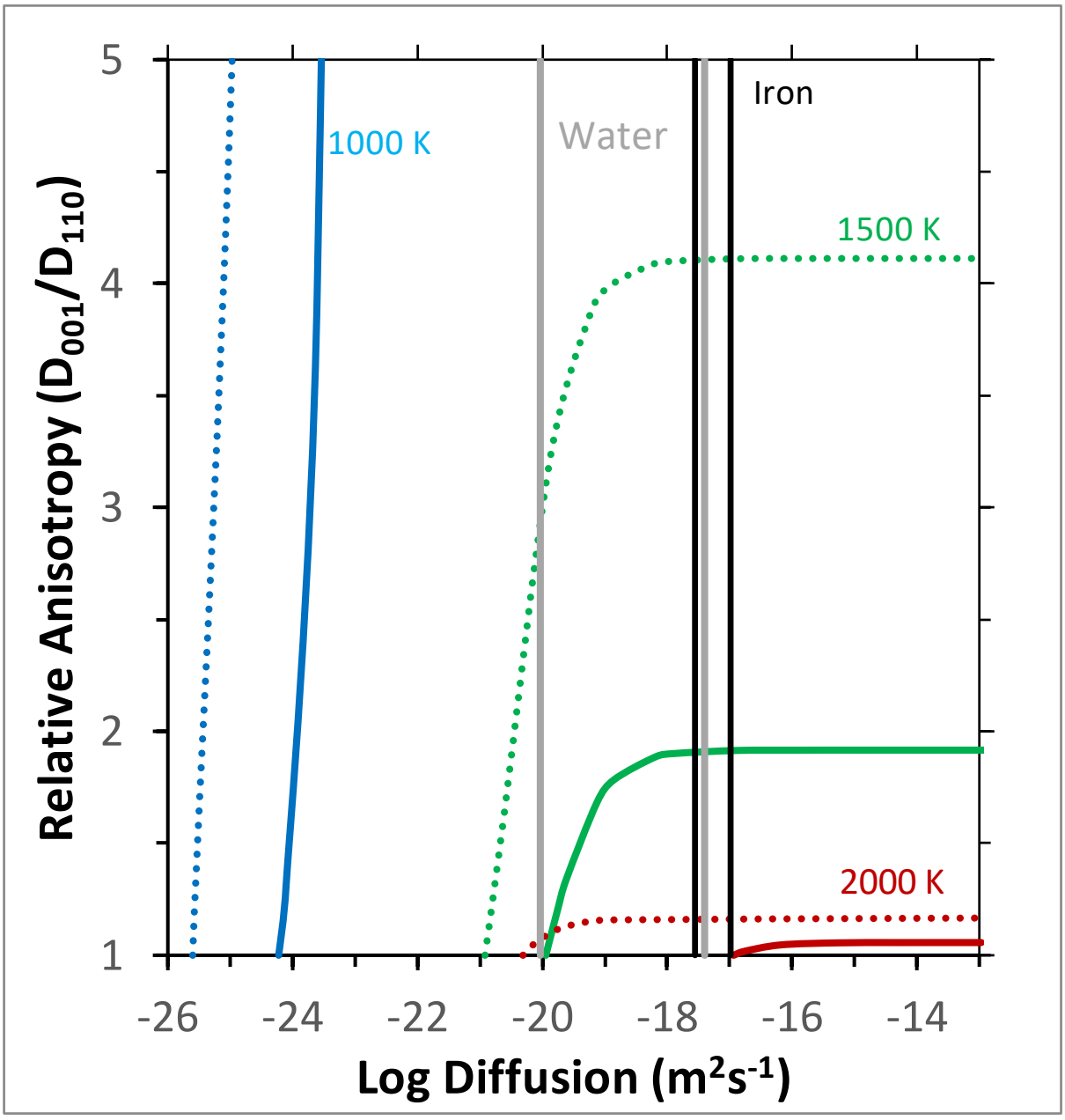

Fig 8 Comparision of anisotropy (defined as diffusion in the [001] direction/ diffusion in the [110] direction) for different diffusion rates (D_x) in a system of self diffusion+extrinsic vacancies. Anistropy is relative to pure forsterite which is 1. This was determined by solving Equation 9 as a function of diffusion rate. Lines are at 1000 K (blue), 1300 K (green) and 1600 K (red) and solid lines represent 5 GPa, dotted lines 10 GPa (uncorrected) which correct to around 1 and 6 GPa respectively.

The two black lines represent the range of D_x between Fe=1-20% for olivine at 0 GPa, 1300 K and $fO^2=10^{-7}$ Dohmen and Chakraborty (2017). The two light lines represents the range of D_x for water ranging between 1-150 wt. ppm at ~8 GPA and 1300 K (Fei *et al.* 2018).

	0 GPa	5	10
	Formation Energy (eV)		
0 K	5.65	6.43	6.54
1000	4.94	5.96	6.37
1300	4.73	5.78	6.27
1600	4.52	5.60	6.13
	Vacancy Concentration		
1000	4.13×10^{-13}	3.06×10^{-15}	9.23×10^{-17}
1300	8.51×10^{-10}	8.81×10^{-12}	9.37×10^{-13}
1600	9.59×10^{-08}	2.14×10^{-09}	2.89×10^{-10}

Table 1: Free energy of the Frenkel reaction at various pressures and temperatures and the corresponding concentration of vacancies and interstitials (in defects/unit cell) in a pure forsterite crystal where only the Mg Frenkel reaction forms significant defects- this concentration is for each defect type so the concentration of total defects (vacancies + interstitials) is twice this number.

		Vacancy		Interstitial	
		E_a (eV)	ν^* (Hz)	E_a (eV)	ν^* (Hz)
Hops from M1 Site					
A/G	M1-M1	0.75	1.01×10^{13}	3.22	9.11×10^{08}
B/H	M1-M1	4.12	3.71×10^{15}	3.16	1.22×10^{10}
C/I	M1-M2/I2	1.45	2.37×10^{14}	0.59	3.01×10^{09}
I*	M1-I2			1.35	2.38×10^{08}
D/J	M1-M2/I2	1.91	4.39×10^{14}	0.56	2.02×10^{09}
D*/J*	M1-M2/I2	1.91	4.39×10^{14}	1.29	2.80×10^{09}
Hops From M2/I2 Site					
C/I	M2/I2-M1	0.45	1.15×10^{14}	0.39	1.41×10^{13}
I*	M1-I2			1.15	1.11×10^{12}
D/J	M2/I2-M1	1.00	2.13×10^{14}	0.36	9.46×10^{12}
D*/J*	M2/I2-M1	1.00	2.13×10^{14}	1.09	1.31×10^{13}
E/K	M2/I2-M2/I2	1.65	4.27×10^{14}	1.08	5.53×10^{12}
F/L	M2/I2-M2/I2	2.82	2.31×10^{15}	N/A	N/A

Table 2: Activation energy and modified attempt frequency v* of various hops (shown in Figure 1 and 3 with the hop distances outlined in Table S4 and S8) for forsterite at 0 GPa uncorrected. Hop L could not be stabilised but is very high in energy. Hops with an asterisk go in the reverse direction where this is not equivalent.

		[100]	[010]	[001]	[001] 5 GPa	[001] 10 GPa
Vacancy	1000 K	1.58×10^{-14}	6.61×10^{-14}	1.91×10^{-10}	1.88×10^{-10}	1.88×10^{-10}
	1300	3.37×10^{-12}	1.42×10^{-11}	1.48×10^{-09}	1.27×10^{-09}	1.19×10^{-09}
	1600	9.15×10^{-11}	4.02×10^{-10}	5.71×10^{-09}	5.30×10^{-09}	4.93×10^{-09}
Interstitial	1000	3.47×10^{-13}	7.58 X 10-13	2.65×10^{-13}	6.13×10^{-12}	6.66×10^{-11}
	1300	1.39×10^{-12}	3.62 X 10-12	1.18×10^{-12}	1.39×10^{-11}	8.44×10^{-11}
	1600	3.83×10^{-12}	7.86 X 10-12	3.96×10^{-12}	2.46×10^{-11}	1.01×10^{-10}

Table 3: Diffusion coefficients (m^2/s) of vacancies and interstitials in three directions at 0 GPa (uncorrected) with 5 and 10 GPa (uncorrected) [001] diffusion coefficients also listed. For the other coefficients in [100] and [010] at 5 and 10 GPa see Table S10 and S11.